X-ray Spectroscopy Characterization of Electronic Structure and Metal-Metal Bonding in Dicobalt Complexes

Arun S. Asundi[1], Roel L. M. Bienenmann[2], Daniël L. J. Broere[2], Ritimukta Sarangi[1]

[1]*Stanford Synchrotron Radiation Lightsource, SLAC National Accelerator Laboratory, Menlo Park, CA 94025, USA*

[2]*Organic Chemistry and Catalysis, Institute for Sustainable and Circular Chemistry, Faculty of Science, Utrecht University, Universiteitsweg 99, 3584 CG, Utrecht, The Netherlands*

Abstract

Developing multimetallic complexes with tunable metal-metal interactions has long been a target of synthetic inorganic chemistry efforts, due to the unique and desirable properties that such compounds can exhibit. However, understanding the relationship between metal-metal bonding and chemical properties in multimetallic compounds has been challenging due to system-dependent factors that can influence metal-metal and metal-ligand interactions including ligand identity, coordination geometry, and metal-metal distance. Moreover, experimental investigations often provide only indirect information about metal-metal bonding while direct experimental insight into orbital overlap is lacking. In this work we apply a combination of X-ray absorption and emission spectroscopy and quantum chemical calculations to describe the electronic structure and bonding properties in a series of dicobalt complexes supported by expanded pincer PNNP ligands. In the compounds with a pseudo-octahedral coordination geometry, a single Co-Co σ-bond forms, for which we directly characterize both the σ-bonding and σ*-antibonding molecular orbitals via their strong contributions to the Co K-edge X-ray emission and absorption

spectra, respectively. In contrast, the dicobalt complexes with a pseudo-tetrahedral coordination environment do not exhibit Co-Co bonding, due to symmetry constraints on orbital overlap and the 3d orbital occupancies of Co^{2+} ions in a tetrahedral ligand field. We extend the spectroscopically-driven insights into Co-Co bonding to diiron(II) (d^6) complexes to develop conditions necessary for metal-metal σ-bonding to occur. We show that strong overlap of atomic orbitals with appropriate symmetry (*e* in tetrahedral ligand field, e_g in octahedral ligand field) is a necessary condition for metal-metal σ-bonding to occur. Finally, we demonstrate how the orbital overlap arguments can be applied to related dicobalt complexes to resolve uncertainties regarding the presence or absence of a Co-Co bond in these species. This work highlights how fundamental insights into electronic structure and bonding through X-ray spectroscopy uncover important factors governing metal-metal interactions and guide the rational design of multimetallic complexes with tunable metal-metal bonds.

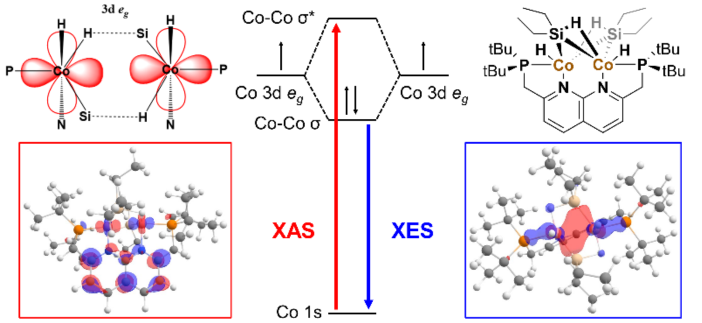

1. Introduction

The design of organometallic complexes is increasingly trending towards multimetallic species, especially those in which the metals are in close contact.[1–3] These systems gain unique chemical and electronic properties through heterometallic interactions,[4,5] mixed valency,[6,7] and metal-metal bonding,[8,9] which are not available in monometallic systems. As a result, multimetallic systems have potential in numerous processes, including molecular catalysis,[10–12] separations,[13] small molecule activation,[14,15] and magnetic applications.[16,17] For example, charge transfer between metals can influence the electronic structure and chemical properties of these sites, as reported by Cammarota *et al.* in a series of Ni-M complexes (M = Al, Ga, In) for H_2 binding.[18] The authors showed that H_2 binding to Ni occurs through σ donation to the vacant Ni(0) $4p_z$ orbital, which becomes energetically accessible through charge transfer from Ni to the neighboring metal. The effect of Ni-M charge transfer on Ni $4p_z$ energy and the resulting strength of H_2 bonding increased with the size of the trivalent group 13 metal. A similar effect was reported by Moore *et al.* for the hydrogenation of aryl C-F bonds by Rh-In catalysts.[19] The reaction proceeds through a formal Rh^{1-}/Rh^{1+} redox cycle, enabled through stabilization of the Rh^{1-} intermediate through a Rh → In charge transfer interaction. Multimetallic systems can also exhibit unique properties via the cooperative binding of different metal sites to a substrate. For example, Isnard *et al.* examined ring-opening polymerization of lactic acids by a series of dinuclear aluminum complexes.[20] The authors proposed a mechanism in which the Al-bound O of a growing polymer chain attacks the ester of a lactic acid monomer bound to the neighboring Al site, enabling ring-opening. The resulting polymer chain is transferred to the new Al site, and chain growth continues through a shuttling mechanism between the two Al sites. Multimetallic centers are also found in biological systems, in which metal-metal interactions often play a key role in tuning highly efficient catalytic processes.[21–26] Moreover, these naturally occurring systems facilitate chemical transformations extremely efficiently using earth-abundant 3d transition metals, in contrast to synthetic organometallic catalysts, which typically feature a single metal atom and often require the use of expensive and scarce 4d and 5d transition metals to achieve similar performance.[27,28] Thus, understanding bonding and developing multimetallic complexes with tunable metal-metal interactions have long been goals in the study of organometallic systems.

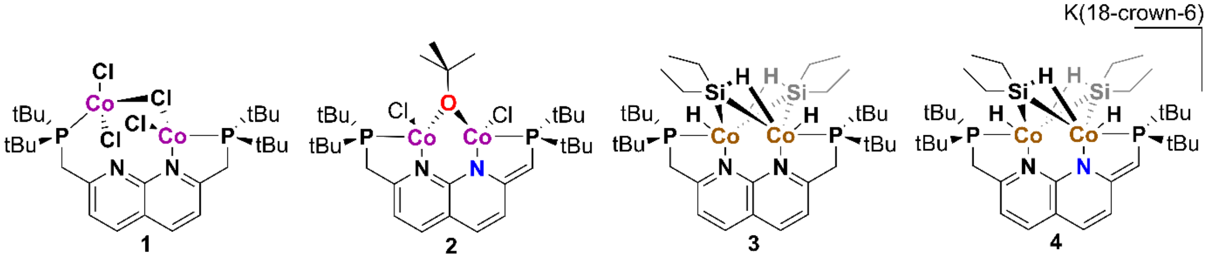

Figure 1. Dicobalt compounds studied in this work.

In this work, we describe the electronic properties and bonding in four dicobalt complexes supported by a PNNP expanded pincer ligand (Figure 1).[29] In all compounds Co is in nominal 2+ oxidation state. However, in **3** and **4**, there is uncertainty regarding the oxidation states of Co, whose electronic structures may be significantly perturbed by charge transfer between the metals or with the ligands. The PNNP ligand is neutral in **1** and **3**, and mono-anionic (due to deprotonation of the one of the methylene linkers) in **2** and **4.** Compound **4** is derived from **3** by a single deprotonation of the PNNP ligand, but it is unclear whether deprotonation results in an internal redox process between Co and the PNNP ligand. In addition to understanding the electronic properties specific to these species, this set of complexes is well-suited to a broader investigation of multiple factors that affect Co-Co interactions, including coordination geometry, ligand strength, and Co-Co distance. Recently, two structures similar to **3** and **4** have been reported in the literature by the groups of Deng and Nakajima.[30,31] In both cases, the complexes are supported by mononucleating *N*-heterocyclic carbene (NHC) ligands and feature multiple bridging silane moieties. Whether there is a Co-Co bond present in these structures is not well established, the authors of both studies base arguments about the presence (Nakajima *et al.*) or absence (Deng *et al.*) of a Co-Co bond in their complexes mainly on the observed Co-Co distance and the diamagnetic nature of these molecules. However, direct experimental or computational evidence for such a bond is absent.

We investigate the electronic structure and bonding in **1** – **4** using X-ray absorption and emission spectroscopy (XAS and XES) and (time-dependent) density functional theory (DFT and TD-DFT) calculations. Although X-ray spectroscopy studies of organometallic (including bimetallic) systems are common, insights into metal-metal bonding are often deduced only from metal-metal distance extracted from the extended X-ray absorption fine structure (EXAFS), with only a few reports of direct characterization of orbital interactions. In one such example Hadt *et al.* showed that the Co K-pre-edge XAS of Co(IV) centers in Co_4O_4 clusters contained a feature attributed to oxygen-mediated metal-metal interactions in the cuboidal core.[32] In a computational report, Zhang *et al.* calculated valence-to-core XES of dicobalt and diiron species, and identified a transition associated with metal-metal σ-bonding orbitals,[33] suggesting the possibility of observing and quantifying these transitions experimentally. Here, we characterize Co-ligand and Co-Co interactions in **1** – **4** using Co K-edge XAS and XES, which experimentally probe the valence empty and filled levels, respectively, furnishing detailed electronic structure insights and direct evidence for Co-Co σ-bonding.[34–39] Using DFT, we construct the molecular orbital description to substantiate the experimentally-observed spectral features.[40–42] We extend the knowledge gained from the electronic characterization of these compounds to establish a set of criteria for metal-metal σ-bond formation considering ligand identity, coordination geometry, and d-electron count. Finally, we apply these insights to the compounds described by Deng and Nakajima to resolve the uncertainties around the presence or absence of Co-Co σ-bonding in each case.

2. Results and Analysis

2.1. Spin State by Co Kβ Mainline XES

^{1}H NMR Evans method measurements show that **1** and **2** are paramagnetic (septet), indicative of two high-spin (s = 3/2) Co^{2+} centers, whereas **3** and **4** are diamagnetic species.[29] To confirm these spin assignments, we performed Co Kβ XES measurements, which provides site-specific spin-state information. The Kβ mainline spectrum is composed of the $K\beta_{1,3}$ and Kβ' peaks.[35,43,44] In systems with unpaired d-electrons, the energy position and splitting between these features is modulated by p-d exchange interactions. In closed-shell systems, the Kβ' features is not observed. For this analysis, we compare the Kβ XES of **1** – **4** with high-spin ($Co^{II}(acetate)_2$) and low-spin ($Co^{III}(acac)_3$, acac = acetylacetonate) references. $Co^{III}(acac)_3$ was chosen as a reference for the Co^{2+} compounds in this study due to the better representation of the singlet electronic structure by the low-spin d^6 Co^{3+} reference than by a low-spin d^7 Co^{2+} species (doublet). Note that small differences in peak positions and spectral lineshapes between the dicobalt complexes and reference compounds results from differences in oxidation state and ligands.[44] **1** and **2** exhibit asymmetry in the $K\beta_{1,3}$ feature (~7648.5 eV) and a pronounced low-energy shoulder from the Kβ' (~7637.5 eV), which are characteristic of high-spin Co^{2+} species (Figure 2).[45] In contrast, the spectra for **3** and **4** show features characteristic of singlet Co centers, with the $K\beta_{1,3}$ feature (~7647.2 eV) showing minor asymmetry at lower energy due to coupling of the 3p hole with a closed-shell valence electron configuration.

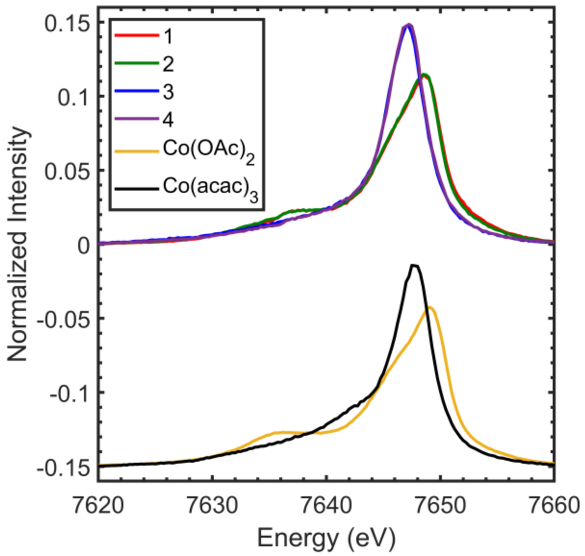

Figure 2. Co K$\beta_{1,3}$ X-ray emission spectra for dicobalt compounds and references; High-spin $Co(OAc)_2$; low-spin $Co(acac)_3$.

The high-spin Co^{2+} natures of **1** and **2** are unsurprising, since a tetrahedral ligand field results in a weak d-orbital splitting and rarely produces low-spin species.[46,47] However, low-spin singlet electronic configuration assignments of **3** and **4** are unusual due to the odd electron count of the nominally Co^{2+} centers (d^7). This may be explained by (1) formation of a Co-Co bond via overlap of the singly occupied 3d orbital on each Co center, (2) ligand mediated spin-pairing of the unpaired electrons, or less likely, (3) charge transfer between Co centers resulting in a mixed valence compound (e.g. $Co^{1+}Co^{3+}$).

2.2. Valence Characteristics from Co K-edge XAS and XES

Co K-edge XAS measurements were performed to characterize the vacant Co-based valence electronic structure (Figure 3). **1** and **2** exhibit a pre-edge feature that is well-separated from other rising edge contributions and is consistent with Co^{2+} in a tetrahedral coordination environment.[48–50] Deconvolution reveals that the pre-edge for each spectrum is composed of an intense feature at 7709.3 eV, with greater intensity for **2** than **1**, and a low-intensity shoulder at ~7711.4 eV (Figure S1, Table S1). In **3** and **4**, the pre-edge features occur ~2 eV higher in energy and overlap significantly with other rising-edge contributions, limiting our ability to quantify differences in energy and intensity. Therefore, high energy resolution fluorescence detected (HERFD) XAS data were measured to better resolve the pre-edge features (Figure 3b). While the intensity mechanism in HERFD-XAS is not directly comparable to standard XAS,[51] the data show similar energy and intensity trends to the standard XAS measurements, indicating that a significant fraction of the contribution to the standard XAS is captured in the HERFD-XAS. The low-energy transitions for **3** and **4** are better resolved in the HERFD-XAS data. The HERFD-XAS pre-edge regions were deconvoluted to identify dominant contributions to the observed spectral shapes, and the resulting components were used to guide the deconvolution of the standard Co K-pre-edges (Figure S2, Table S2). In **3** and **4**, the highest intensity pre-edge transition appears at ~7710.8 eV, 1.5 eV higher than the most intense pre-edge feature in **2** (Note: we are careful to not refer to this energy difference as a "peak shift" because the features in **1** and **2** originate from different transitions than those in **3** and **4**, as will be discussed below). The Co K-pre-edges for **3** and **4** also show low-intensity features at 7709.3 eV in both compounds.

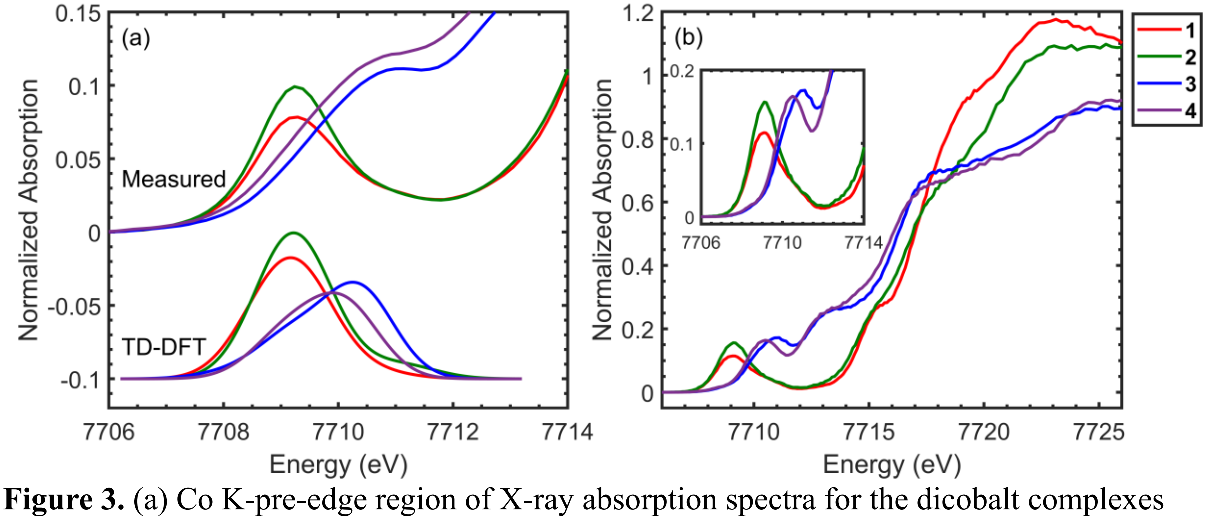

Figure 3. (a) Co K-pre-edge region of X-ray absorption spectra for the dicobalt complexes along with TD-DFT computed pre-edge transitions. (b) Co K-edge HERFD-XAS measurements on dicobalt complexes. Inset shows the expanded pre-edge region.

Co-ligand bonding interactions were further investigated using Co Kβ valence-to-core (v2c) XES (Figure 4). The spectra of **1** and **2** exhibit broad features at ~7703-7706 eV and a low-energy tail towards ~7699 eV, with no significant differences between these compounds. In contrast, the spectra for **3** and **4** are much more intense. Deconvolution of the spectra reveals strong contributions from features at ~7705.5 eV, ~7703.0 eV, and ~7699.9 eV, indicating that the ligand system in **3** and **4** enables emission at these energies from Co-based MOs that are not present in the tetrahedrally coordinated complexes **1** and **2** (Figure S3, Table S3).

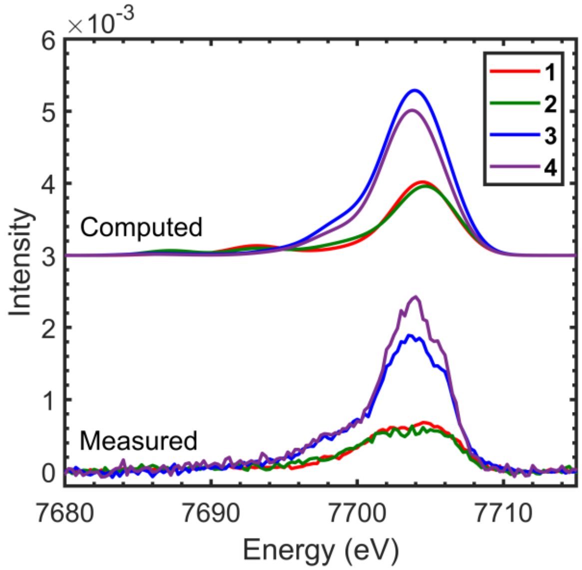

Figure 4. Background subtracted Co Kβ valence-to-core XES for dicobalt complexes along with DFT-computed emission spectra.

2.3. Computed Geometric and Electronic Structures

Spin unrestricted DFT geometry optimization was performed on **1** – **4** assuming singlet, triplet, and septet spin states. Singlet and septet configurations have similar energies for **1** and **2**, achieved in both cases by high-spin Co centers with opposite (singlet) or equivalent (septet) spin densities (Table S4). The singlet state is most stable for **3** and **4**, with no spin density on either Co site. These results agree with the Co Kβ XES and ^{1}H NMR Evans method measurements. The DFT-optimized bond lengths for all compounds agree well with those measured by X-ray crystallography and Co K-edge EXAFS (Tables S5, S6), confirming the structural validity of the DFT model.

Computed Co K-edge XAS and v2c XES by TD-DFT are in excellent agreement with the experimental spectra (Figures 3, 4). The TD-DFT Co K-pre-edge spectra of **1** and **2** show several transitions centered around 7709.3 eV contributing to a high-intensity feature, and a few low-intensity contributions centered around 7711 eV, consistent with the high energy tail observed in the experimental spectra (Figures S4, S5). In **3** and **4**, the most intense computed transitions are observed at 7710.4 eV and lower intensity contributions are present at 7709.3 eV, in line with the observed spectral trends (Figures S6, S7). The computed v2c XES likewise show a significantly higher intensity for **3** and **4** compared to **1** and **2**. These results confirm that the valence electronic structures of these complexes are accurately modeled by DFT at the def2-TZVP/BP86 level of theory.

2.4. Valence Electronic Structure and Bonding

Molecular orbital bonding descriptions were obtained from the DFT-optimized structures. Bonding and electronic structures of **1** and **2** are similar, with minor variations due to ligand differences. The highest energy occupied valence MOs consist of Cl 3p, Co 3d and P 3p levels, which are intermixed and spread over a range of occupied MOs (Figure S8). Co-based orbitals also weakly overlap with the Cl 3s (and O 2p and O 2s in **2**) levels. The unoccupied valence MOs contain two contributions. The first set of vacant MOs consist of Co 3d orbitals with t_2 symmetry, which are singly-occupied. Second, the π* MOs on the PNNP ring system overlap with occupied Co 3d levels. This back-bonding interaction leads to a small percentage of Co 3d character mixed into the PNNP π* system, with an orbital energy higher than the Co 3d t_2 vacant orbitals.

In contrast, there are three interactions specific to the low-spin d^7 species **3** and **4** that most strongly differentiate their electronic structures from **1** and **2**. The first factor is a change in the coordination geometry around the Co centers. In **3** and **4**, each Co mononuclear fragment has an approximately trigonal bipyramidal geometry, with axial terminal hydride and N ligands and with P, Si, and bridging hydride in the equatorial plane. In this geometry, the Co 3d orbitals transform as a_1' ($3d_{z^2}$), e' ($3d_{x^2-y^2}$, $3d_{xy}$), and e'' ($3d_{xz}$, $3d_{yz}$), with a_1' significantly destabilized due to direct overlap with the axial ligands. In the dinuclear complex, the neighboring Co distorts the final geometry towards a pseudo-octahedral structure, resulting in energetic convergence of the $3d_{xy}$, $3d_{xz}$, and $3d_{yz}$ orbital energies (t_{2g} symmetry) and destabilization of $3d_{x^2-y^2}$ towards the $3d_{z^2}$ level (e_g symmetry). The O_h symmetry allows for overlap of the Co $3d_{x^2-y^2}$ orbitals, which are oriented along the Co-Co axis. Calculations show the formation of a Co-Co σ-bond, which stabilizes the Co $3d_{x^2-y^2}$ based MO ~1.2 eV lower in energy than the average Co 3d t_{2g} (Figure 5). A corresponding Co-Co σ*-antibonding MO is observed in the vacant valence levels. Co-Co Mayer bond orders of 0.31 (**3**) and 0.28 (**4**) are consistent with a moderate Co-Co interaction and are higher than in **1** and **2** (values of 0.12 and 0.14, respectively). Lastly, strong σ overlap between Co $3d_{z^2}$ and the terminal H 1s is observed, resulting from the short Co-H bond distance of about 1.48 Å. The Co-H σ-bond results in an occupied Co $3d_{z^2}$ – H 1s based MO 1.0 eV lower in energy than the Co-Co σ-bonding MO, and a vacant σ*-antibonding MO 1.3 eV higher than the Co-Co antibonding MO (Figure 5).

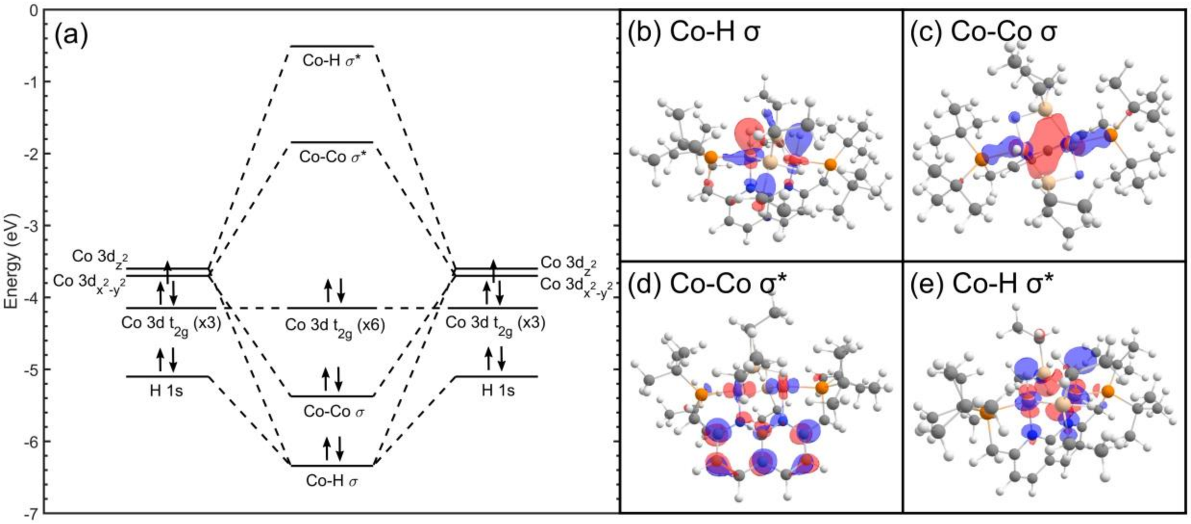

Figure 5. (a) MO diagram of compound **3** depicting orbital interactions between Co-Co and Co-H (terminal). Representative contour plots of MOs are shown for (b) Co-H σ-bonding, (c) Co-Co σ-bonding, (d) Co-Co σ*-antibonding, and (e) Co-H σ*-antibonding interactions.

The differences in MO descriptions are directly reflected in the spectral variations. The Co K-pre-edges in **1** and **2** arise from different types of transitions from those in **3** and **4**. Specifically, the intense feature at 7709.3 eV in **1** and **2** results from 1s-to-3d based transitions consistent with high-spin Co^{2+} compounds (Figures 6, S4, S5).[48–50] The high-energy shoulder ~7711.3 eV is assigned to transitions to the dominantly PNNP ring π* based MOs, which contain a small amount of Co character through back-bonding. On the other hand, in **3** and **4**, the low-intensity transition at 7709.3 eV results from transitions to the σ*-antibonding MO formed by Co-Co $3d_{x^2-y^2}$ orbital overlap (Figures 6, S6, S7). This feature is similar in energy to the corresponding transition in **1** and **2**, consistent with the assignment of **3** and **4** as Co^{2+} species, with no redox change at Co due to deprotonation of the PNNP ligand. (Table S8). The lower intensity of this transition compared to **1** and **2** follows the well-understood difference between tetrahedral and octahedral species, driven by a decrease in 3d-4p hybridization in the more centrosymmetric octahedral complexes. The feature at 7710.8 eV in **3** and **4** results from transitions to the Co $3d_{z^2}$ – H 1s σ* MO (Figures 6, S6, S7), whose energy destabilization by 1.5 eV relative to the Co $3d_{x^2-y^2}$ vacancy agrees with the DFT computed MO description.

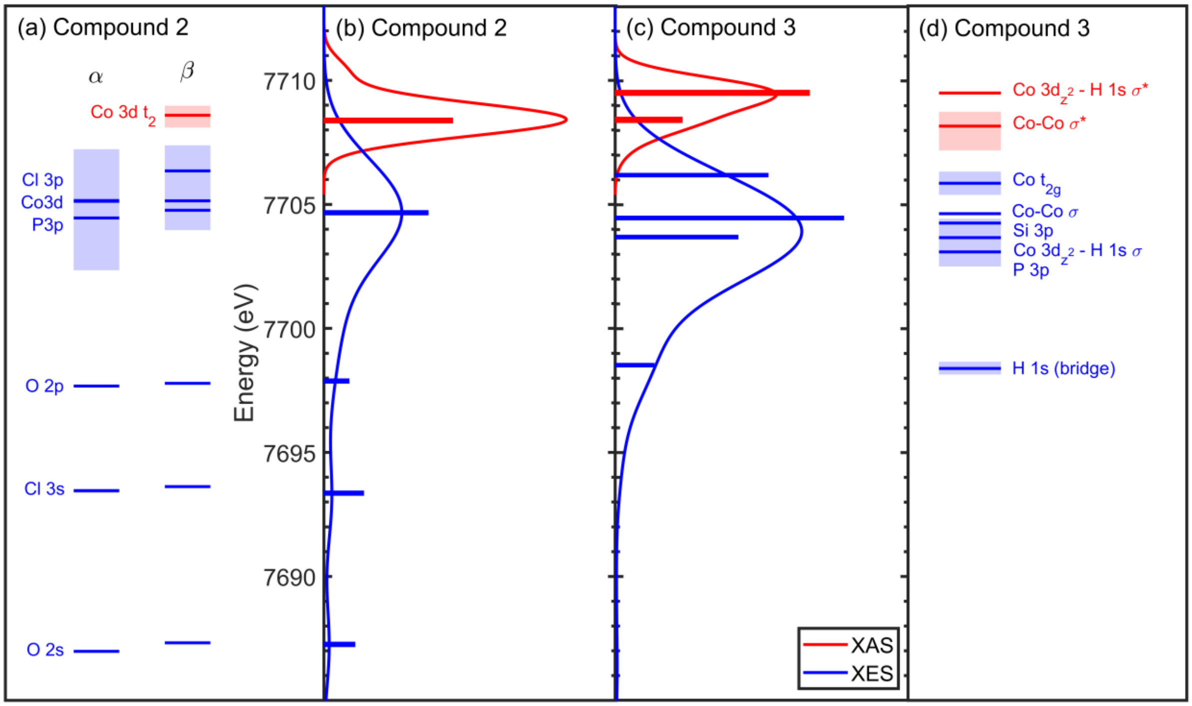

Figure 6. (a), (d) Valence MO diagram for compounds **2** and **3** showing occupied (blue) and vacant (red) MOs. Light blue and red shaded regions show the range of MO energies attributed to each MO type. Computed Co K-edge XAS and XES with dominant transitions are shown for (b) **2** and (c) **3**.

The computed v2c XES for **1** and **2** show transitions from 7701-7707 eV due to Co 3d *e*, Co 3d t_2, P 3p and Cl 3p based MOs, which are highly mixed with each other (Figures 6, S9, S10). The low energy shoulder ~7699.9 eV represents transitions from N 2p and for **2**, O 2p levels. Computed Co Kβ v2c emission spectra for **3** and **4** reveal that the increase in intensity relative to **1** and **2** is driven by a few key transitions, the most intense of which is from the Co-Co σ-bonding MO described above (Figures 6, S11, S12). The high Co 4p character in this donor MO leads to the intense feature at ~7703.0 eV. Another intense contribution results from the Co $3d_{z^2}$ – H 1s based bonding MO at ~7699.9 eV. Finally, the high-energy emission feature at ~7705.6 eV is assigned to transitions from occupied Co 3d t_{2g} levels. The Co K-edge XAS and

Kβ v2c XES probe Co-Co and Co-H interactions from both the bonding and antibonding MO perspectives, and taken together, provide direct evidence of a Co-Co σ-bond in **3** and **4**. It is important to note that computational methods alone (QTAIM, NBO, NLMO/NPA) often provide ambiguous and conflicting results on the presence of Co-Co bonds in these compounds (see discussion in SI, Figure S13).

3. Discussion

3.1. Symmetry Requirements for Co-Co σ-Bonding and Effect on Spin State

Spin state difference between septet **1** and **2** and singlet **3** and **4** can be attributed to three factors: (1) difference in type of ligands between Cl^-/$tBuO^-$ versus $Si(C_2H_5)_2$/H^-, (2) pseudo-tetrahedral versus pseudo-octahedral geometry, and (3) shorter inter-Co distance leading to Co-Co σ-bond formation. The magnitudes of these factors in determining spin state were assessed by considering energetic differences arising from changes in ligand identity and coordination geometry (full discussion in supporting information). In these compounds, spin state is most strongly affected by the binding of hydride ligands in **3** and **4**, while the change in coordination geometry plays a smaller but still significant role, consistent with expectations from ligand field theory.

The effect of Co-Co distance and bonding is inferred from relaxed scan calculations of compounds **2** and **3** with varying Co-Co distances (Figure S15). For **3** as the Co-Co distance increases towards that in **2**, the energy increases by ~14 kcal/mol, due to decreased Co $3d_{x^2-y^2}$ orbital overlap and a weaker Co-Co σ-bond. Interestingly, the opposite behavior is observed for **2**, with an increase in energy by ~5 kcal/mol when the Co-Co distance decreases towards that in **3**. This result indicates that even when the Co centers are brought close together in **2**, a Co-Co σ-bond does not form. The difference in Co-Co bonding behavior between **2** and **3** arises from the symmetry requirements for d-orbital overlap in the different coordination geometries and has important implications for the possibilities of metal-metal σ-bonding.

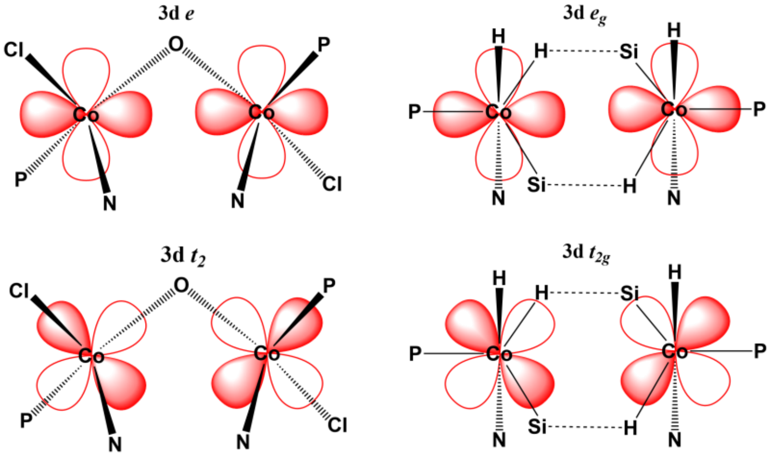

Figure 7. Schematic of 3d orbital orientation in tetrahedral (left) and octahedral (right) coordination environments of **2** and **3**. Selected orbitals with *e* and t_2 (tetrahedral) and e_g and t_{2g} (octahedral) symmetry are depicted.

To understand how 3d orbitals overlap in a bimetallic complex with tetrahedral ligand configuration, we consider the relative orientations of the 3d orbitals with *e* and t_2 symmetry. As shown in Figure 7, the Co 3d orbitals with *e* symmetry have the appropriate orientation for σ-overlap, whereas the t_2 orbitals allow for π- and δ-bonding. A tetrahedral mononuclear fragment must contain one or more singly-occupied *e* orbital for σ-bonding to occur in the resulting bimetallic complex. In the case of high-spin Co^{2+} (d^7) species, the *e* symmetry orbitals on each Co center are fully occupied, and thus do not participate in Co-Co σ-bonding. This symmetry constraint explains the lack of Co-Co σ-bonding in **2**. As we have shown, σ-bonding for octahedrally coordinated metal centers results from overlap of the 3d orbitals with e_g symmetry, such as in the low-spin Co^{2+} (d^7) species **3** and **4** (Figure 7).

3.2. Metal-Metal σ-Bonding Requirements and Predictions for Diiron Complexes

Metal-metal σ-bond formation depends on several interactions, including ligand-field splitting of d-orbitals, energy stabilization of metal-metal σ-bonding orbitals, and electron spin alignment energy. Here, we extend our characterization of the dicobalt species to systems with different d-electron counts, with computational investigation of a diiron(II) (d^6) analogue of **3**. We consider only σ-bonding, for which we have experimental evidence with the dicobalt complexes. We further note that considering bimetallic analogues with much lower or higher d-electron counts may be purely hypothetical, as such species may not exist.

From the symmetry arguments above, if the orbitals with *e* symmetry (tetrahedral) or e_g symmetry (octahedral) are fully occupied, no metal-metal σ-bonding is expected. In a high-spin tetrahedral system this is the case for d^7-d^{10} metals, and in octahedral species, this is true for d^{10} metals.[*] For a mononuclear fragment with singly-occupied *e* (tetrahedral) or e_g (octahedral) orbitals, metal-metal σ-bonding in the dinuclear complex is possible, as observed for the octahedral dicobalt complex **3**. This condition is satisfied for high-spin d^1-d^6 metals in a tetrahedral geometry suggesting the possibility of metal-metal σ-bond formation in such complexes. A similar pattern is observed in dinuclear Ni(I) (d^9) complexes in a square-planar geometry, where a single Ni-Ni σ-bond forms due to the appropriate symmetry of the singly occupied $3d_{x^2-y^2}$ orbitals.[52] While this condition is necessary for metal-metal σ-bond formation, it may not be a sufficient requirement, and further study is needed on systems with singly occupied orbitals with appropriate symmetry for σ-bonding.

For a octahedral species that may be expected to have vacant e_g symmetry orbitals (as is the case for low-spin d^1-d^6 metals), metal-metal σ-bonding in the dinuclear complex is still

---

[*] Different conclusions may be drawn depending on the ligand system. For example, in the ligand system of **3** and **4** where the $3d_{z^2}$ orbital is destabilized by strong hydride overlap, metal-metal σ-bonding is likely inaccessible for d^8 metals, since vacancy in the $3d_{z^2}$ level forces full occupancy of the $3d_{x^2-y^2}$ orbitals oriented along the metal-metal axis.

possible, as long as the σ overlap stabilizes the bonding MO below the energy of the t_{2g} orbitals. We illustrate this by computing the ground state of a diiron(II) analogue of **3**. The triplet state of the diiron complex is the most stable and results in an Fe-Fe distance of 2.626 Å (Table S9). Spin densities around 0.69 and Hirshfeld charges around -0.10 are similar on the two Fe centers, showing that the triplet state does not result from electron transfer between the Fe sites. Instead, the Mayer bond order of 0.43 suggest the formation of a weak Fe-Fe bond, similar to that in the dicobalt complexes, and examination of valence MO contour plots reveals an occupied σ-bonding MO and a vacant σ*-antibonding MO, analogous to those observed in the dicobalt complex **3** (Figure S16). Thus, just as Co-Co σ-bonding in **3** and **4** results in the unexpected lack of spin density on the d^7 Co^{2+} centers, calculations for a diiron analogue of **3** suggest that Fe-Fe σ-bonding leads to a triplet state and non-zero spin density on the d^6 Fe^{2+} sites.

3.3. Assessment of Bonding in Related Dicobalt Silane Complexes

The groups of Deng and Nakajima have reported the synthesis and characterization of dicobalt complexes similar to **3** and **4**.[30,31] In both cases the Co centers have formal 2+ oxidation states, contain bridging and terminal silane and hydride ligands, and are supported by N-heterocyclic carbene ligands. However, the studies differed in their assessment of the existence of a Co-Co bond. Complex **10** reported by Deng et al. (referred to here as **D10**) was found to be diamagnetic based on ^{1}H Evan's method NMR spectroscopy but based on the crystal structure Co-Co distance of 2.58 Å, the authors suggested a weak Co-Co interaction. In contrast, diamagnetic complex **4** by Nakajima et al. (referred to here as **N4**) possessed a Co-Co distance of 2.45 Å and was concluded to have a single Co-Co bond. Here, we explain the differences in Co-Co bonding for **D10** and **N4** by extending the orbital overlap arguments presented above.

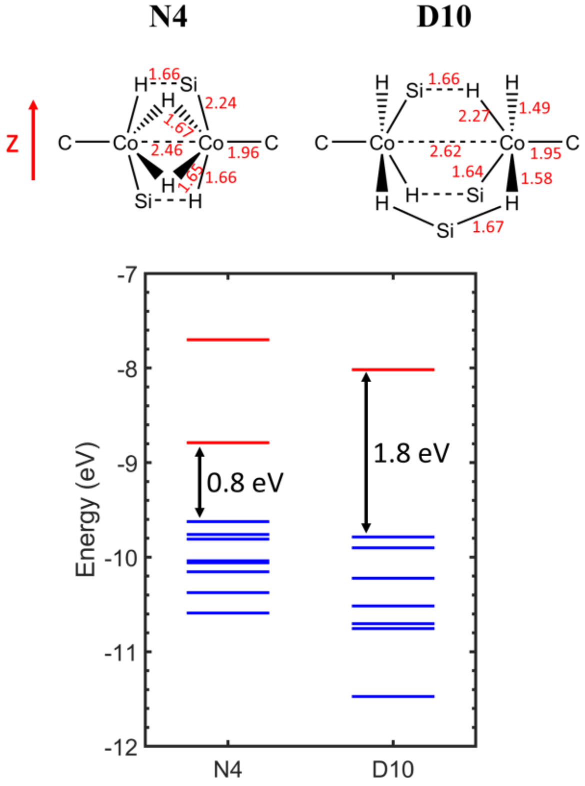

Figure 8. Schematic of the dicobalt core structures of compounds **N4** and **D10** with bond lengths listed in Å. C and Si refer to *N*-heterocyclic carbene and silane ligands, respectively, the coordinate with Co. Valence Co 3d-based MO energies are shown with occupied MOs in blue and vacant MOs in red. Energies are referenced to a methyl C 1s at -275 eV.

DFT optimizations on **D10** and **N4** were performed at the same level of theory as for **1** – **4**. The optimized Co-Co distances for **D10** (2.62 Å) and **N4** (2.46 Å) reproduce experimental trends (Figure 8). Both calculations converged to a singlet ground state with zero spin density on all atoms. Co-Co Mayer bond orders of 0.78 (**N4**) and <0.1 (**D10**) are consistent with a single bond in **N4** and no bond in **D10**. Notably **3** is intermediate between **N4** and **D10**, with a Co-Co distance of 2.55 Å and Mayer bond order of 0.31. Additionally, broken symmetry calculations show high magnitude negative J-couplings for **3**, **4**, **N4**, and **D10** (Table S10). These values are much larger than those typical for antiferromagnetically coupled metal centers and are consistent with closed-shell electron configurations for these compounds.[53]

Unsurprisingly, one contributing factor to the change in Co-Co bond strength is the Co-Co distance. The trend in bond order (**D10** < **3** < **N4**) is consistent with an increase in orbital overlap that would result from a decrease in Co-Co distance. To assess the magnitude of the Co-Co distance effect, we performed constrained geometry optimization calculations on **D10** and **N4** with the Co-Co distance fixed at the values for the other compound. When the Co-Co distance in **D10** is decreased to 2.46 Å, the Mayer bond order increases to 0.14, still significantly lower than that of **N4**. When the Co-Co distance in **N4** is increased to 2.62 Å, the bond order decreases to 0.40, a substantial drop but still much higher than that of **D10**. Thus, while Co-Co distance strongly impacts bond strength, it does not in itself imply a bonding interaction.

Differences in ligand strength and coordination geometry also play an important role in governing Co-Co σ-bonding. Like the dicobalt compounds in this study, both **N4** and **D10**, feature Co centers in an approximately trigonal bipyramidal environment, which distort towards octahedral symmetry due to the neighboring Co in the equatorial plane (Figures 8, S17). In **N4** each Co has H (1.660 Å) and Si (2.243 Å) axial ligands while the equatorial ligands are C (1.960 Å) and two H's (1.650 Å and 1.666 Å). The Co $3d_{xy}$ orbitals are significantly destabilized by overlap with bridging hydrides in the equatorial plane and are thus vacant. Like **3** and **4**, the $3d_{x^2-y^2}$ orbitals of each Co overlap, allowing a single Co-Co σ-bond to form. The difference in Co-Co bond order between **N4** (0.78) and **3** (0.31) likely results from differences in coordination geometry, which may allow for greater orbital overlap in **N4** than in **3**. This difference also highlights that metal-metal bonding is best described by a continuous extent of interaction, rather than a discrete whole number of metal-metal bonds.

The Co centers in **D10** are also in trigonal bipyramidal geometry with axial H (1.65 Å) and Si (2.27 Å) ligands and equatorial C (1.95 Å) and two hydrides (1.49 Å and 1.58 Å) (Figures

8, S17). Compared to **N4**, distances to the equatorial hydride ligands are much shorter and overlap significantly more with the Co $3d_{x^2-y^2}$ orbital due to geometric differences between bridging hydrides (**N4**) and bridging silanes (**D10**) (Figures 8, S17). Thus in **D10**, the Co $3d_{x^2-y^2}$ orbitals are strongly destabilized by overlap with hydrides and remain vacant, preventing Co-Co σ-bond formation. Despite the absence of the Co-Co σ-bond, **D10** is diamagnetic, indicating that all electrons are paired. Computed valence MO energies show that the HOMO-LUMO gap is 1.0 eV larger for **D10** than **N4** (Figure 8), indicating a much stronger ligand field, and consistent with the large negative J-coupling for this compound (Table S10). The resulting destabilization of the LUMO forces electron pairing, leading to a closed-shell ground state. The nature of interactions leading to electron pairing are unclear, due to variations in bond lengths and angles around Co, which lead to low-symmetry Co centers and significant intermixing of the Co 3d valence levels. We postulate the presence of a multi-center 2-electron bond, mediated by the bridging silane ligands, which have been previously proposed in multimetallic complexes featuring Si-based ligands.[54,55] To visualize this interaction, MOs were computed for a simplified analogue of **D10**, in which phenyl groups were replaced with methyls. This analogue shows multiple occupied MOs with spin density shared between the Co and bridging silanes, consistent with a multicentered bonding interaction (Figure S18).

4. Conclusion

Through a combination of X-ray spectroscopy and supporting calculations, we have developed a detailed understanding of bonding and electronic structure in a series of dicobalt complexes supported by PNNP expanded pincer ligands. The dicobalt species in a pseudo-octahedral coordination environment supported by diethylsilane and hydride ligands show clear evidence of a Co-Co σ-bonding interaction, which has been characterized from both the occupied (σ-bonding) and vacant (σ*-antibonding) perspectives. This metal-metal σ-bonding results from symmetry-allowed overlap of the singly occupied Co $3d_{x^2-y^2}$ orbitals, and leads to the formation of an electron pair in an energetically stabilized bonding MO. In these complexes, the hydride ligands have a significant impact on electronic structure, resulting from strong overlap with the vacant Co $3d_{z^2}$ orbital. In contrast the dicobalt complexes in a tetrahedral coordination environment do not exhibit Co-Co σ-bonding, even when both Co centers are bound in the PNNP pocket. This lack of bonding is explained by the Co 3d orbitals with *e* symmetry in a tetrahedral ligand field, which have the appropriate orientation for σ-bonding, but are fully occupied for high-spin Co^{2+} (d^7) ions.

We have used spectroscopically-driven insights into the factors enabling or preventing metal-metal σ-bonding in dicobalt complexes to extend knowledge of metal-metal σ-bonding in two ways. First, we proposed conditions for metal-metal σ-bond formation depending on coordination geometry and d-electron count and used these criteria to evaluate bonding in diiron(II) analogues of the complexes in this study. Second, we applied the arguments of orbital symmetry and ligand strength to explain the presence or absence of a Co-Co σ-bond in two related dicobalt compounds with silane and hydride ligands similar to those in this study. The strength and geometry of the ligand field alter the relative stability of Co 3d orbitals, thus changing the occupancy of the orbitals with appropriate symmetry for σ-overlap, which either allows or prohibits Co-Co σ-bond formation. Overall, the insights into Co-Co interactions gained through X-ray spectroscopy enable us to understand energetic factors that contribute to metal-metal interactions and rationally predict which bimetallic species could exhibit σ-bonding. This effort provides valuable guidance to synthetic chemists, who can use the requirements and criteria discussed here to target development efforts towards organometallic complexes with desirable properties and metal-metal interactions.

5. Methods

5.1. Experimental Methods

Synthesis and structural characterization of PNNP ligand and dicobalt complexes by single-crystal XRD and EXAFS are described in reference [29]. Co K-edge X-ray absorption spectra were measured at the Stanford Synchrotron Radiation Lightsource (SSRL) on the unfocused 20-pole 2T wiggler beamline 7-3 under standard ring conditions (3 GeV, ~500 mA). A liquid N_2-cooled Si(220) double crystal monochromator was used for energy selection with crystal orientation of $\varphi = 90°$. Samples were handled in a dry N_2-filled glovebox. Bulk solid samples were prepared by grinding ~5 mg sample (mass calculated to yield ~1 absorption length above the Co K-edge) with ~25 mg dry boron nitride in an agate mortar and pestle to form a uniformly colored, fine powder. The sample was pressed into a 7 mm diameter cylindrical pellet and held between 64 μm pieces of Kapton tape. During measurement, samples were loaded into a Cryo Industries closed-cycle liquid He cryostat and maintained at ~10 K throughout the measurement. Data was collected in transmission mode using N_2-filled ionization chambers. The X-ray beam size was 1 mm (height) × 5 mm (width) for all measurements. Spectra were measured to $k = 14.1$ Å^{-1} and a Co foil was measured simultaneously for energy calibration, with the first inflection point in the Co foil spectrum fixed at 7709 eV.

Co K-edge HERFD-XAS, $K\beta_{1,3}$ XES, and $K\beta_{v2c}$ XES measurements were performed at SRL on the undulator beamline 15-2 under standard ring conditions. The beam was focused using a bent single-crystal KB mirror, and energy selection was achieved using a liquid N_2-cooled Si(111) double-crystal monochromator. To minimize self-absorption effects, the compounds were measured as dilute bulk powders, prepared by grinding the sample with dry boron nitride (~1:100 mass ratio of sample to boron nitride) to a uniform, fine powder. ~30 mg of powder was used to prepare cylindrical pellets as described above. During the measurement, samples were held in an Oxford liquid He cryostat at a temperature of ~10 K. A custom He-filled bag was used as a beam flightpath to minimize absorption and scattering of the incident beam and fluorescence photons from air. Each measurement was performed on a different sample spot to ensure that replicate spectra were not influenced by sample beam damage. The incident and transmitted beam intensities were measured using N_2-filled ionization chambers. HERFD-XAS measurement were collected using a 7-crystal Johann-type hard X-ray spectrometer tuned to the Co Kα emission line (6930.2 eV).[56] A Co foil was measured simultaneously for energy calibration. Co Kβ emission spectra were collected with the incident X-ray beam fixed at 8100 eV. The emission spectrum energy was calibrated by setting the Co foil Kβ mainline to 7649.4 eV.

Standard and HERFD Co K-edge XAS data processing was done in the Athena program of the Demeter package.[57] Standard Co K-edge and HERFD Co K-edge spectra presented here were obtained by averaging 2 and 5 replicate scans on different sample spots, respectively. Linear pre-edge and post-edge lines were used for baseline subtraction to obtain normalized absorption spectra. XAS deconvolution was performed in Matlab using Gaussian components with varying energy and peak heights. The widths of the components were allowed to vary but were constrained to be the same value of all Gaussian components. Pre-edge fits were performed using the lsqcurvefit function in Matlab to minimize the sum of squared residuals between the measured and modeled spectra. The fitting procedure was performed with several initial guess values for the peak heights and energies to ensure that the optimized parameters represented a global minimum.

Co K$\beta_{1,3}$ and Kβ_{v2c} emission spectra were analyzed in Matlab. Linear background functions were subtracted from the Kβ mainline spectra and a cubic spline was used to model the background of the valence-to-core spectra. The intensities of the Kβ mainline spectra were scaled to an integrated intensity of 1. The low-energy region of the v2c spectra were scaled to overlay with the high-energy region of the normalized Kβ mainline spectra in the energy range 7654.5-7663.5 eV to normalized the v2c region. The normalized v2c spectra were deconvoluted using Gaussian components in Matalb using the lsqcurvefit function to minimize the sum of squared residuals between the measured and modeled spectra. The Gaussian components had variable heights and energies; the widths were also allowed to vary but were fixed to be the same value for all components. Fitting was performed with several initial guess values for the peak heights and energies to ensure that the optimized parameters represented a global minimum.

5.2. Computational Methods

Spin-unrestricted density functional theory calculations were performed using ORCA 5.0.3.[58] Geometry optimization was performed for all experimentally characterized and hypothetical compounds discussed in this work. The BP86 exchange-correlation functional was employed and the redefinition of Ahlrichs triple-ζ split-valence basis set def2-TZVP was used for geometry optimization and spectra calculations.[59,60] For the NBO and QTAIM calculations, structures of **3** and **4** were optimized as restricted singlets using the Gaussian 16 revision C01 software package.[61] Optimized geometries were validated to be energetic minima by the absence of negative vibrational frequencies. Calculations were performed at the BP86/def2-TZVP level of theory unless specified otherwise, in which case the 6-311G(d,p) triple-ζ People basis set or the redefinition of Ahlrichs double-ζ split-valence basis set (def2-SVP) was used.[62–65] Grimme DFT-3 empirical dispersion correction with Becke-Johnson damping was employed in all calculations.[66] The NBO calculations were performed with the NBO 6.0 software.[67] QTAIM calculations and their visualizations were performed using the MultiWFN program.[68] TD-DFT calculations of X-ray absorption transitions from the Co level, and DFT calculations of X-ray emission transitions to the Co 1s level were performed using the DFT-optimized atomic coordinates. Effects of spin-orbit coupling were included in the emission calculations by setting DoSOC to "true" in ORCA. A tight convergence requirement was imposed for all calculations. The calculated pre-edge and emission transitions were expressed as Gaussian functions with half-widths of 0.85 eV (Co K-edge XAS) and 1.55 eV (Co $K\beta_{v2c}$ XES) to account for core-hole and instrument broadening. The computed transition energies were shifted by 196.2 eV (Co K-edge XAS) and 195.4 eV (Co $K\beta_{v2c}$ XES) to compensate for the inaccuracies in DFT-calculated core-hole potentials.[41] Contour plots of the molecular orbitals associated with the absorption and emission transitions were visualized from the DFT output using Chemcraft 1.8 and their compositions were extracted from the DFT output using MOAnalyzer 1.61.[69]

Associated Content

The supporting information is available free of charge at [URL].

Discussion of metal-metal bonding using other computational techniques; Deconvolution of X-ray spectra; computational X-ray spectra and MOs associated with transitions; MO compositions relevant to X-ray spectra; relaxed scan calculation energies; structure, bonding parameters, and MO contour plots for diiron and **D10** analogues.

Notes

The authors declare no competing financial interest.

Acknowledgements

A. S. A. and R. S. are supported by the U. S. Department of Energy, Office of Energy Efficiency and Renewable Energy (EERE), Advanced Manufacturing Office (AMO), and Bioenergy Technologies Office (BETO) as part of the BOTTLE Consortium, funded under Contract No. DE-AC36-08GO28308 with the National Renewable Energy Laboratory. R. L. M. B. and D. L. J. B. are supported by The Netherlands Organization of Scientific Research (VI. Veni 192.074 to D. L. J. B.). Stanford Synchrotron Radiation Lightsource, SLAC National Accelerator Laboratory, is supported by the U. S. Department of Energy, Office of Science, Office of Basic Energy Sciences. The SSRL Structural Molecular Biology Program is supported by the DOE Office of Biological and Environmental Research and by the National Institutes of Health, National Institutes of General Medical Sciences (P30GM133894). This work made use of the Dutch national e-infrastructure with the support of the SURF Cooperative using grans No. EINF-1254, EINF-3520, and EINF-737. The authors thank Matthew Latimer, Leah Kelly, Erik Nelson, and Thomas Kroll for beamline support for the measurements performed in this work.

References

(1) Berry, J. F.; Thomas, C. M. Multimetallic Complexes: Synthesis and Applications. *Dalton Trans.* **2017**, *46* (17), 5472–5473.
(2) Berry, J. F.; Lu, C. C. Metal-Metal Bonds: From Fundamentals to Applications. *Inorg. Chem.* **2017**, *56* (14), 7577–7581.
(3) Fianchini, M.; Mikhailov, O. V. Introduction from Guest Editors to Special Issue "Multi-Metallic Systems: From Strong Cooperative Bonds to Weak M-M Interactions." *Int. J. Mol. Sci.* **2022**, *23* (19).
(4) Chipman, J. A.; Berry, J. F. Paramagnetic Metal-Metal Bonded Heterometallic Complexes. *Chem. Rev.* **2020**, *120* (5), 2409–2447.
(5) Buchwalter, P.; Rosé, J.; Braunstein, P. Multimetallic Catalysis Based on Heterometallic Complexes and Clusters. *Chem. Rev.* **2015**, *115* (1), 28–126.
(6) Gould, C. A.; Randall McClain, K.; Reta, D.; C Kragskow, J. G.; Marchiori, D. A.; Lachman, E.; Choi, E.-S.; Analytis, J. G.; David Britt, R.; Chilton, N. F.; Harvey, B. G.; Long, J. R. Ultrahard Magnetism from Mixed-Valence Dilanthanide Complexes with Metal-Metal Bonding. *Science* **2022**, *375*, 198–202.

(7) Launay, J. P. Mixed-Valent Compounds and Their Properties – Recent Developments. *Eur. J. Inorg. Chem.* **2020**, *2020* (4), 329–341.

(8) Fang, W.; Zhu, Q.; Zhu, C. Recent Advances in Heterometallic Clusters with F-Block Metal-Metal Bonds: Synthesis, Reactivity and Applications. *Chem. Soc. Rev.* **2022**, *51* (20), 8434–8449.

(9) Joy, J.; Danovich, D.; Kaupp, M.; Shaik, S. Covalent vs Charge-Shift Nature of the Metal-Metal Bond in Transition Metal Complexes: A Unified Understanding. *J. Am. Chem. Soc.* **2020**, *142* (28), 12277–12287.

(10) Maity, R.; Birenheide, B. S.; Breher, F.; Sarkar, B. Cooperative Effects in Multimetallic Complexes Applied in Catalysis. *ChemCatChem* **2021**, *13* (10), 2337–2370.

(11) Yolsal, U.; Shaw, P. J.; Lowy, P. A.; Chambenahalli, R.; Garden, J. A. Exploiting Multimetallic Cooperativity in the Ring-Opening Polymerization of Cyclic Esters and Ethers. *ACS Catal.* **2024**, 1050–1074.

(12) Sciortino, G.; Maseras, F. Computational Study of Homogeneous Multimetallic Cooperative Catalysis. *Top. Catal.* **2022**, *65* (1–4), 105–117.

(13) Yang, X.; Xu, Q. Bimetallic Metal-Organic Frameworks for Gas Storage and Separation. *Cryst. Growth Des.* **2017**, *17* (4), 1450–1455.

(14) Wang, Q.; Brooks, S. H.; Liu, T.; Tomson, N. C. Tuning Metal-Metal Interactions for Cooperative Small Molecule Activation. *Chem. Comm.* **2021**, *57* (23), 2839–2853.

(15) Navarro, M.; Moreno, J. J.; Pérez-Jiménez, M.; Campos, J. Small Molecule Activation with Bimetallic Systems: A Landscape of Cooperative Reactivity. *Chem. Comm.* **2022**, *58* (80), 11220–11235.

(16) Jiang, L.; Feng, X. L.; Lu, T. B.; Gao, S. Synthesis, Structures, and Magnetic Properties of a Series of Cyano-Bridged Fe-Mn Bimetallic Complexes. *Inorg. Chem.* **2006**, *45* (13), 5018–5026.

(17) Coronado, E.; Galan-Mascaros, J. R.; Marti-Gastaldo, C. Design of Bimetallic Magnetic Chains Based on Oxalate Complexes: Towards Single Chain Magnets. *Cryst. Eng. Comm.* **2009**, *11* (10), 2143–2153.

(18) Cammarota, R. C.; Xie, J.; Burgess, S. A.; Vollmer, M. V.; Vogiatzis, K. D.; Ye, J.; Linehan, J. C.; Appel, A. M.; Hoffmann, C.; Wang, X.; Young, V. G.; Lu, C. C. Thermodynamic and Kinetic Studies of H_2 and N_2 Binding to Bimetallic Nickel-Group 13 Complexes and Neutron Structure of a Ni(H_2-H_2) Adduct. *Chem. Sci.* **2019**, *10* (29), 7029–7042.

(19) Moore, J. T.; Lu, C. C. Catalytic Hydrogenolysis of Aryl C-F Bonds Using a Bimetallic Rhodium-Indium Complex. *J. Am. Chem. Soc.* **2020**, *142* (27), 11641–11646.

(20) Isnard, F.; Lamberti, M.; Lettieri, L.; D'Auria, I.; Press, K.; Troiano, R.; Mazzeo, M. Bimetallic Salen Aluminum Complexes: Cooperation between Reactive Centers in the Ring-Opening Polymerization of Lactides and Epoxides. *Dalton Trans.* **2016**, *45* (40), 16001–16010.

(21) Ghosh, A. C.; Duboc, C.; Gennari, M. Synergy between Metals for Small Molecule Activation: Enzymes and Bio-Inspired Complexes. *Coord. Chem. Rev.* **2021**, *428*, 213606.

(22) Land, H.; Senger, M.; Berggren, G.; Stripp, S. T. Current State of [FeFe]-Hydrogenase Research: Biodiversity and Spectroscopic Investigations. *ACS Catal.* **2020**, *10* (13), 7069–7086.

(23) Birrell, J. A.; Rodríguez-Maciá, P.; Reijerse, E. J.; Martini, M. A.; Lubitz, W. The Catalytic Cycle of [FeFe] Hydrogenase: A Tale of Two Sites. *Coord. Chem. Rev.* **2021**, *449*.

(24) Caserta, G.; Hartmann, S.; Van Stappen, C.; Karafoulidi-Retsou, C.; Lorent, C.; Yelin, S.; Keck, M.; Schoknecht, J.; Sergueev, I.; Yoda, Y.; Hildebrandt, P.; Limberg, C.; DeBeer, S.; Zebger, I.; Frielingsdorf, S.; Lenz, O. Stepwise Assembly of the Active Site of [NiFe]-Hydrogenase. *Nat. Chem. Biol.* **2023**, *19* (4), 498–506.

(25) Barber, J. Mn_4Ca Cluster of Photosynthetic Oxygen-Evolving Center: Structure, Function and Evolution. *Biochem.* **2016**, *55* (42), 5901–5906.

(26) Gerey, B.; Gouré, E.; Fortage, J.; Pécaut, J.; Collomb, M. N. Manganese-Calcium/Strontium Heterometallic Compounds and Their Relevance for the Oxygen-Evolving Center of Photosystem II. *Coord. Chem. Rev.* **2016**, *319*, 1–24.

(27) Komarova, A. A.; Perekalin, D. S. Noble Metal versus Abundant Metal Catalysts in Fine Organic Synthesis: Cost Comparison of C-H Activation Methods. *Organometallics* **2023**, *42* (13), 1433–1438.

(28) Macchioni, A. Speciality Grand Challenges in Organometallic Catalysis. *Front. Catal.* **2021**, 1:704925.

(29) Bienenmann, R. L. M.; Asundi, A. S.; Lutz, M.; Sarangi, R.; Broere, D. L. J. Chloride, Alkoxide or Silicon: The Bridging Ligand Dictates the Spin-State in Dicobalt Expanded Pincer Complexes. *Submitted.*

(30) Sun, J.; Gao, Y.; Deng, L. Low-Coordinate NHC-Cobalt(0)-Olefin Complexes: Synthesis, Structure, and Their Reactions with Hydrosilanes. *Inorg. Chem.* **2017**, *56* (17), 10775–10784.

(31) Ishizaka, Y.; Nakajima, Y. Synthesis and Characterization of Silyl-Bridged Dinuclear Cobalt Complexes Supported by an N-Heterocyclic Carbene. *Organometallics* **2019**, *38* (4), 888–893.

(32) Hadt, R. G.; Hayes, D.; Brodsky, C. N.; Ullman, A. M.; Casa, D. M.; Upton, M. H.; Nocera, D. G.; Chen, L. X. X-Ray Spectroscopic Characterization of Co(IV) and Metal-Metal Interactions in Co_4O_4: Electronic Structure Contributions to the Formation of High-Valent States Relevant to the Oxygen Evolution Reaction. *J. Am. Chem. Soc.* **2016**, *138* (34), 11017–11030.

(33) Zhang, Y.; Bergmann, U.; Schoenlein, R.; Khalil, M.; Govind, N. Double Core Hole Valence-to-Core X-Ray Emission Spectroscopy: A Theoretical Exploration Using Time-Dependent Density Functional Theory. *J. Chem. Phys.* **2019**, *151* (14).

(34) Penner-Hahn, J. E. X-Ray Absorption Spectroscopy in Coordination Chemistry. *Coord. Chem. Rev.* **1999**, 1101–1123.

(35) DeGroot, F. High-Resolution X-Ray Emission and X-Ray Absorption Spectroscopy. *Chem. Rev.* **2001**, *101* (6), 1779–1808.

(36) Sarangi, R. X-Ray Absorption near-Edge Spectroscopy in Bioinorganic Chemistry: Application to $M-O_2$ Systems. *Coord. Chem. Rev.* **2013**, *257* (2), 459–472.

(37) Atkins, A. J.; Bauer, M.; Jacob, C. R. High-Resolution X-Ray Absorption Spectroscopy of Iron Carbonyl Complexes. *Phys. Chem. Chem. Phys.* **2015**, *17* (21), 13937–13948.

(38) McLoughlin, E. A.; Giles, L. J.; Waymouth, R. M.; Sarangi, R. X-Ray Absorption Spectroscopy and Theoretical Investigation of the Reductive Protonation of Cyclopentadienyl Cobalt Compounds. *Inorg. Chem.* **2019**, *58* (2), 1167–1176.

(39) Delgado-Jaime, M. U.; Debeer, S.; Bauer, M. Valence-to-Core X-Ray Emission Spectroscopy of Iron-Carbonyl Complexes: Implications for the Examination of Catalytic Intermediates. *Chem. Eur. J.* **2013**, *19* (47), 15888–15897.

(40) Besley, N. A. Density Functional Theory Based Methods for the Calculation of X-Ray Spectroscopy. *Acc. Chem. Res.* **2020**, *53* (7), 1306–1315.

(41) Besley, N. A. Modeling of the Spectroscopy of Core Electrons with Density Functional Theory. *WIREs Comput. Mol. Sci.* **2021**, 11:e1527.

(42) Bokarev, S. I.; Kühn, O. Theoretical X-Ray Spectroscopy of Transition Metal Compounds. *WIREs Comput. Mol. Sci* **2020**, 10:e1433.

(43) Lafuerza, S.; Carlantuono, A.; Retegan, M.; Glatzel, P. Chemical Sensitivity of Kβ and Kα X-Ray Emission from a Systematic Investigation of Iron Compounds. *Inorg. Chem.* **2020**, *59* (17), 12518–12535.

(44) Pollock, C. J.; Delgado-Jaime, M. U.; Atanasov, M.; Neese, F.; Debeer, S. Kβ Mainline X-Ray Emission Spectroscopy as an Experimental Probe of Metal-Ligand Covalency. *J. Am. Chem. Soc.* **2014**, *136* (26), 9453–9463.

(45) Liang, H. W.; Kroll, T.; Nordlund, D.; Weng, T. C.; Sokaras, D.; Pierpont, C. G.; Gaffney, K. J. Charge and Spin-State Characterization of Cobalt Bis(o-Dioxolene) Valence Tautomers Using Co Kβ X-Ray Emission and L-Edge X-Ray Absorption Spectroscopies. *Inorg. Chem.* **2017**, *56* (2), 737–747.

(46) Byrne, E. K.; Richeson, D. S.; Theopold, K. H. Tetrakis(1-Norbornyl)Cobalt, a Low Spin Tetrahedral Complex of a First Row Transition Metal. *J. Chem. Soc., Chem. Commun.* **1986**, 1491–1492.

(47) Jenkins, D. M.; Di Bilio, A. J.; Allen, M. J.; Betley, T. A.; Peters, J. C. Elucidation of a Low Spin Cobalt(II) System in a Distorted Tetrahedral Geometry. *J. Am. Chem. Soc.* **2002**, *124* (51), 15336–15350.

(48) Hunault, M.; Calas, G.; Galoisy, L.; Lelong, G.; Newville, M. Local Ordering around Tetrahedral Co^{2+} in Silicate Glasses. *J. Am. Ceram. Soc.* **2014**, *97* (1), 60–62.

(49) Maurizio, C.; El Habra, N.; Rossetto, G.; Merlini, M.; Cattaruzza, E.; Pandolfo, L.; Casarin, M. XAS and GIXRD Study of Co Sites in $CoAl_2O_4$ Layers Grown by MOCVD. *Chem. Mater.* **2010**, *22* (5), 1933–1942.

(50) Uchikoshi, M.; Shinoda, K. Determination of Structures of Cobalt(II)-Chloro Complexes in Hydrochloric Acid Solutions by X-Ray Absorption Spectroscopy at 298 K. *Struct. Chem.* **2019**, *30* (3), 945–954.

(51) Asakura, H.; Tanaka, T. Recent Applications of X-Ray Absorption Spectroscopy in Combination with High Energy Resolution Fluorescence Detection. *Chem. Lett.* **2021**, *50* (5), 1075–1085.

(52) Zhou, Y. Y.; Hartline, D. R.; Steiman, T. J.; Fanwick, P. E.; Uyeda, C. Dinuclear Nickel Complexes in Five States of Oxidation Using a Redox-Active Ligand. *Inorg. Chem.* **2014**, *53* (21), 11770–11777.

(53) Comba, P.; Hausberg, S.; Martin, B. Calculation of Exchange Coupling Constants of Transition Metal Complexes with DFT. *J. Phys. Chem. A* **2009**, *113* (24), 6751–6755.

(54) Nova, A.; Suh, H. W.; Schmeier, T. J.; Guard, L. M.; Eisenstein, O.; Hazari, N.; Maseras, F. An Unusual Example of Hypervalent Silicon: A Five-Coordinate Silyl Group Bridging Two Palladium or Nickel Centers through a Nonsymmetrical Four-Center Two-Electron Bond. *Angew. Chem Int. Ed.* **2014**, *53* (4), 1103–1108.

(55) Green, J. C.; Green, M. L. H.; Parkin, G. The Occurrence and Representation of Three-Centre Two-Electron Bonds in Covalent Inorganic Compounds. *Chem. Comm.* **2012**, *48* (94), 11481–11503.

(56) Sokaras, D.; Weng, T. C.; Nordlund, D.; Alonso-Mori, R.; Velikov, P.; Wenger, D.; Garachtchenko, A.; George, M.; Borzenets, V.; Johnson, B.; Rabedeau, T.; Bergmann, U. A Seven-Crystal Johann-Type Hard X-Ray Spectrometer at the Stanford Synchrotron Radiation Lightsource. *Rev. Sci. Instrum.* **2013**, *84* (5).

(57) Ravel, B.; Newville, M. ATHENA, ARTEMIS, HEPHAESTUS: Data Analysis for X-Ray Absorption Spectroscopy Using IFEFFIT. *J. Synchrotron Radiat.* **2005**, *12* (4), 537–541.

(58) Neese, F.; Wennmohs, F.; Becker, U.; Riplinger, C. The ORCA Quantum Chemistry Program Package. *J. Chem. Phys.* **2020**, *152* (22).

(59) Becke, A. D. Density-Funnctional Exchange-Energy Approximation with Correct Asymptotic Behavior. *Phys. Rev. A* **1988**, *38* (6) 3098-3100.

(60) Schäfer, A.; Huber, C.; Ahlrichs, R. Fully Optimized Contracted Gaussian Basis Sets of Triple Zeta Valence Quality for Atoms Li to Kr. *J. Chem. Phys.* **1994**, *100* (8), 5829–5835.

(61) Gaussian 16, Revision C.01, Frisch, M. J.; Trucks, G. W.; Schlegel, H. B.; Scuseria, G. E.; Robb, M. A.; Cheeseman, J. R.; Scalmani, G.; Barone, V.; Petersson, G. A.; Nakatsuji, H.; *et al*. Gaussian, Inc., Wallingford CT, 2016.

(62) McLean, A. D.; Chandler, G. S. Contracted Gaussian Basis Sets for Molecular Calculations. I. Second Row Atoms, Z=11-18. *J. Chem. Phys.* **1980**, *72* (10), 5639–5648.

(63) Weigend, F.; Ahlrichs, R. Balanced Basis Sets of Split Valence, Triple Zeta Valence and Quadruple Zeta Valence Quality for H to Rn: Design and Assessment of Accuracy. *Phys. Chem. Chem. Phys.* **2005**, *7* (18), 3297–3305.

(64) Krishnan, R.; Binkley, J. S.; Seeger, R.; Pople, J. A. Self-Consistent Molecular Orbital Methods. XX. A Basis Set for Correlated Wave Functions. *J. Chem. Phys.* **1980**, *72* (1), 650–654.

(65) Raghavachari, K.; Trucks, G. W. Highly Correlated Systems. Excitation Energies of First Row Transition Metals Sc-Cu. *J. Chem. Phys.* **1989**, *91* (2), 1062–1065.

(66) Grimme, S.; Ehrlich, S.; Goerigk, L. Effect of the Damping Function in Dispersion Corrected Density Functional Theory. *J. Comput. Chem.* **2011**, *32* (7), 1456–1465.

(67) Glendening, E. D.; Badenhoop, J. K.; Reed, A. E.; Carpenter, J. E.; Bohmann, J. A.; Morales, C. M.; Karafiloglou, P.; Landis, C. R.; Weinhold, F. NBO 7.0. Theoretical Chemistry Institute, University of Wisconsin: Madison 2018.

(68) Lu, T.; Chen, F. Multiwfn: A Multifunctional Wavefunction Analyzer. *J. Comput. Chem.* **2012**, *33* (5), 580–592.

(69) Delgado-Jaime, M. U.; DeBeer, S. Expedited Analysis of DFT Outputs: Introducing MOAnalyzer. *J. Comput. Chem.* **2012**, *33* (27), 2180–2185.